

Cell–Matrix Interactions Regulate Functional Extracellular Vesicle Secretion from Mesenchymal Stromal Cells

Stephen Lenzini, Koushik Debnath, Jagdish C. Joshi, Sing Wan Wong, Kriti Srivastava, Xue Geng, Ik Sung Cho, Angela Song, Raymond Bargi, James C. Lee, Gary C.H. Mo, Dolly Mehta, and Jae-Won Shin*



Cite This: <https://doi.org/10.1021/acsnano.1c03231>



Read Online

ACCESS |



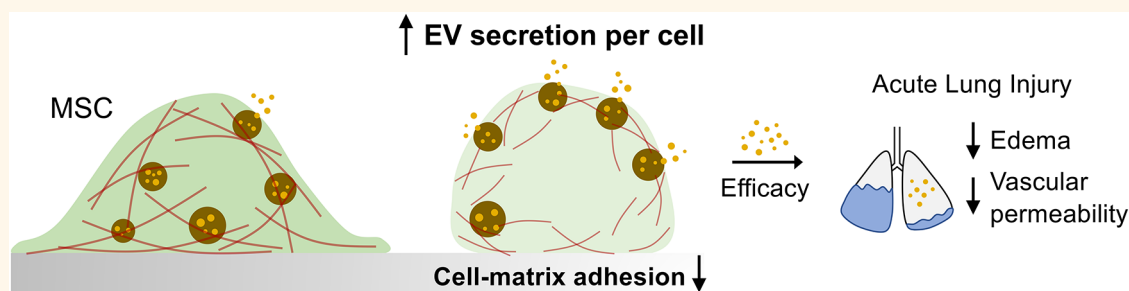
Metrics & More



Article Recommendations



Supporting Information



ABSTRACT: Extracellular vesicles (EVs) are cell-secreted particles with broad potential to treat tissue injuries by delivering cargo to program target cells. However, improving the yield of functional EVs on a per cell basis remains challenging due to an incomplete understanding of how microenvironmental cues regulate EV secretion at the nanoscale. We show that mesenchymal stromal cells (MSCs) seeded on engineered hydrogels that mimic the elasticity of soft tissues with a lower integrin ligand density secrete ~ 10 -fold more EVs per cell than MSCs seeded on a rigid plastic substrate, without compromising their therapeutic activity or cargo to resolve acute lung injury in mice. Mechanistically, intracellular CD63⁺ multivesicular bodies (MVBs) transport faster within MSCs on softer hydrogels, leading to an increased frequency of MVB fusion with the plasma membrane to secrete more EVs. Actin-related protein 2/3 complex but not myosin-II limits MVB transport and EV secretion from MSCs on hydrogels. The results provide a rational basis for biomaterial design to improve EV secretion while maintaining their functionality.

KEYWORDS: extracellular vesicles, hydrogels, nanotherapeutics, biomanufacturing, mechanobiology, mesenchymal stromal cells, tissue injury

Extracellular vesicles (EVs) are cell-secreted nanomaterials composed of a lipid bilayer that are conventionally described as ranging from 50 to 500 nm in diameter.^{1–3}

EVs have emerged as an important class of nanotherapeutics with broad potential to treat various tissue injuries, because they carry therapeutically relevant cargo molecules and deliver to recipient cells.⁴ EVs can also be readily modified to enhance targeting and therapeutic efficacy.⁵ Since EVs are naturally derived from cells, it is important to understand the fundamental mechanisms of EV biogenesis in order to leverage them for manufacturing of therapeutic EVs. EVs are generally classified into subtypes based on their biogenesis pathways in cells. Microvesicles (or ectosomes) are produced by budding directly from the membrane, while intraluminal vesicles (ILVs)

are produced by inward budding within late endosomes that form multivesicular bodies (MVBs).¹ ILVs are then released as exosomes from cells when the MVB fuses with the plasma membrane. Recent studies have established EVs as a critical paracrine secretion mechanism for cell–cell communication.² While physiologically relevant soluble signals, such as hypoxia,⁶

Received: April 16, 2021

Accepted: October 19, 2021

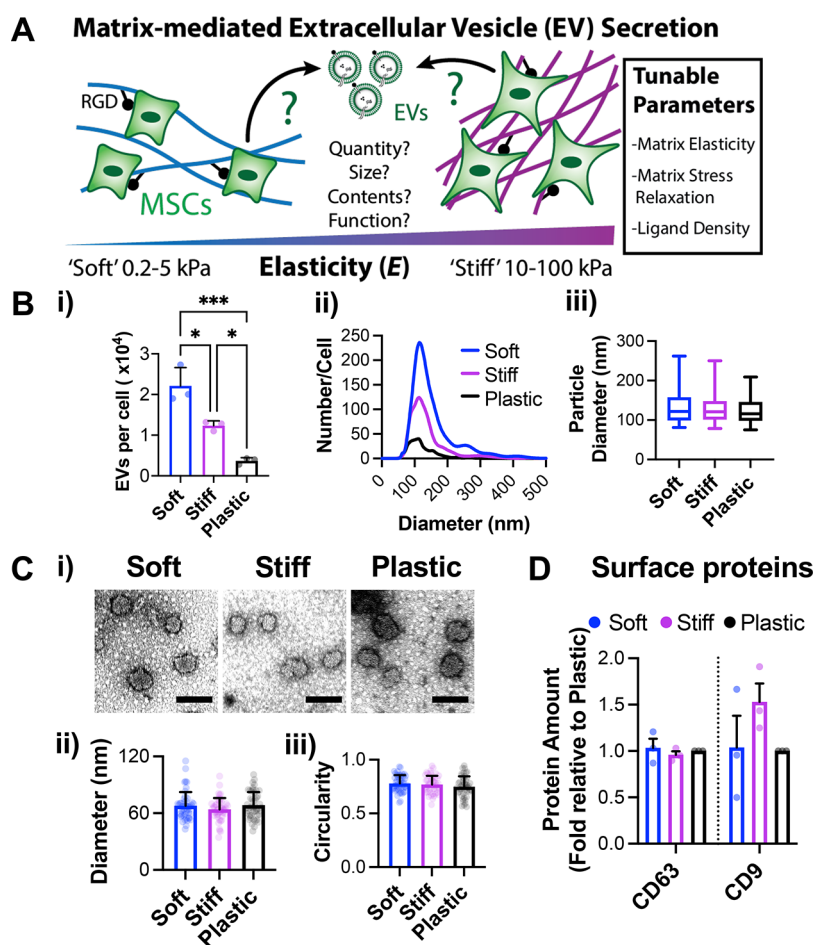


Figure 1. Substrate elasticity determines the amount of EV secretion from MSCs. (A) Illustration of potential biophysical relationships and their impact on EV secretion from MSCs. (B-i) Primary human MSCs produce significantly more EVs on softer elastic alginate hydrogels conjugated with 0.8 mM RGD. Data represent the mean of $N = 3$ experiments. *, $p < 0.05$; ***, $p < 0.001$ via one-way ANOVA with Tukey's post-test. (B-ii) EV size distributions by nanoparticle tracking analysis. Data represent the mean of $N = 3$ particle samples per condition. (B-iii) Quantification of size distribution data in (B-ii). Lines represent the median; the boxes represent the 25–75th percentiles. The whiskers represent the 5–95th percentiles. (C-i) Representative TEM images for secreted vesicles from human MSCs on substrates. Scale bar = 100 nm. (C-ii) Quantification of particle diameter from TEM images. Data are per vesicle measured across $N = 6$ images per condition. (C-iii) Quantification of circularity for vesicles in (C-i). (D) Late endosomal marker protein content measured via ELISA. Data represent the mean of $N = 3$ experiments. For (B), data represent the mean of $N = 3$ experiments. For all, error bars indicate standard error of the mean (SEM).

histamine,⁷ or Ca^{2+} levels⁸ are known to affect EV release, how cellular microenvironments regulate EV biogenesis remains largely unknown.

Mesenchymal stromal cells (MSCs) are known to utilize paracrine secretion mechanisms, including EVs⁹ to communicate with the host and control multiple inflammatory and degenerative conditions.¹⁰ Recent studies show that EVs from MSCs contain therapeutic cargo with bioactive contents that ameliorate lung injury, including angiogenic factors,^{11,12} growth factors,¹³ anti-inflammatory factors,^{14–16} and mitochondrial contents such as mitochondrial DNA (mtDNA).¹⁷ MSCs respond to a variety of signals from microenvironments.¹⁰ In particular, advances in biomaterial design have revealed the sensitivity of MSCs to biophysical properties of the extracellular matrix, which in turn impact cell adhesion, spreading, and differentiation by modulating cytoskeletons.^{18,19} Previous studies suggest that actin cytoskeletons regulate biological processes that affect the plasma membrane surface area or mass, such as exocytosis and endocytosis,²⁰ which may inform the mechanisms of EV biogenesis. However, the role of

matrix biophysical cues in mediating functional EV production at the nanoscale remains unclear.

Since the bone marrow environment from which MSCs are derived presents a diverse range of biochemical and biophysical properties encoded by the extracellular matrix,^{19,21} matrix cues can potentially play a role in determining a level of EV production most appropriate for specific environments. Thus, we hypothesized that cell–matrix interactions determine EV production from MSCs. To test this hypothesis, we leveraged alginate-based hydrogels with a physiologically relevant range of substrate elasticity and integrin–ligand density for MSC mechanosensing.^{22–24} We show that softer hydrogels with less ligand density increase EV production from MSCs due to less integrin activation, while hydrogel stress relaxation does not play a role in this process. Through recombinant fluorescent protein expression and imaging at the nanoscale, we elaborate that MSCs on softer hydrogels exhibit enhanced intracellular CD63⁺ MVB transport, which is correlated with increased fusion of CD63⁺ MVBs with the plasma membrane. Consistent with the notion that less well-developed actin cytoskeletons promote intracellular MVB trafficking and resulting fusion with

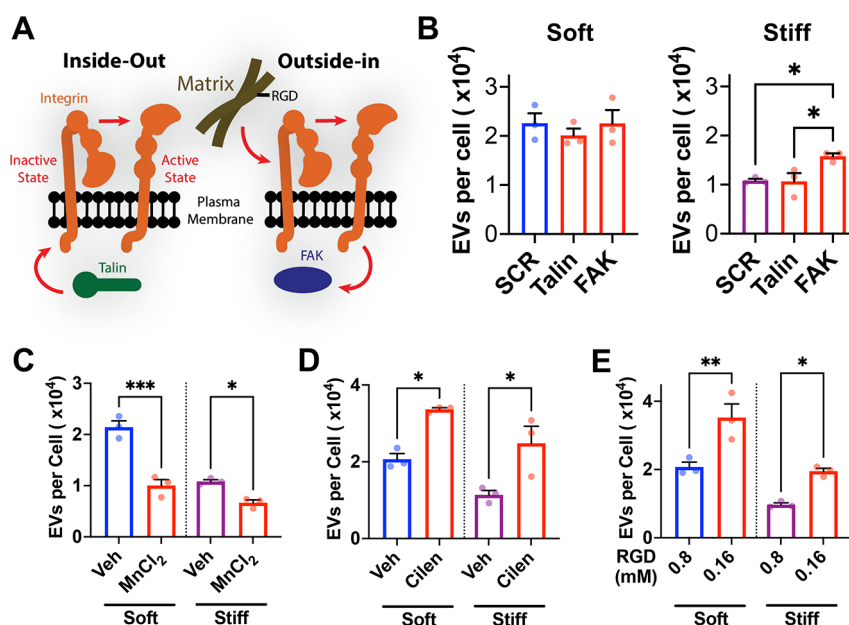


Figure 2. Cell adhesion to substrates through integrin-RGD interaction regulates EV secretion. (A) Illustration of known interactions for integrin inside-out vs outside-in signaling. (B) Treatment of primary human MSCs on substrates with 4 nM siRNA against talin and FAK. (C) Treatment of human MSCs with 3 μ M MnCl₂ or vehicle (veh) during and after adhesion to hydrogels inhibits EV secretion. (D) Treatment of human MSCs with 200 nM cilengitide (cilen) during and after adhesion to hydrogels enhances EV secretion. (E) Decreasing the amount of RGD conjugated in hydrogels significantly increases EV secretion. For (B–E), *, $p < 0.05$; **, $p < 0.01$; ***, $p < 0.001$, via one-way ANOVA with Tukey's post-test, and data represent the mean of $N = 3$ experiments. For all data, error bars indicate the SEM.

the plasma membrane, the inhibition of actin-related protein complex 2/3 (Arp2/3) restores MVB trafficking on the stiffer substrate. Finally, we show that EVs from cells seeded on substrates of different elasticity retain therapeutic efficacy and cargo contents against an animal model of acute lung injury, suggesting that enhanced secretion of EVs on softer substrates does not compromise functionality of EVs.

RESULTS AND DISCUSSION

Substrate Elasticity Determines EV Secretion from MSCs. To test the effect of substrate mechanics on EV secretion from MSCs, we engineered hydrogel substrates comprised of alginate polymer conjugated with the cell adhesion peptide Arg-Gly-Asp (RGD) that binds primarily to $\alpha_4\beta_3$ and $\alpha_5\beta_1$ integrins.²⁵ Alginate-RGD hydrogels can be formed either covalently through adipic acid dihydrazide or physically through divalent cations, resulting in elastic or stress-relaxing hydrogels, respectively²⁶ (Figure S1A). For both types of hydrogels, we considered elastic modulus (Young's modulus) $E \sim 3$ kPa as "soft" and $E \sim 20$ kPa as "stiff" (Figure S1B), values that represent a physiologically relevant range of substrate elasticity for MSC mechanosensing (Figure 1A), while E is ~ 0.1 GPa for conventional plastic substrates.²² We allowed primary human bone marrow MSCs to adhere to substrates for 24 h followed by washout and collection of the serum-free conditioned medium from MSCs after 24 h. After centrifugation of the medium at 10 000g to remove cell, apoptotic, and larger particle fractions,²⁷ particles remaining in the medium were analyzed by nanoparticle tracking analysis and normalized to the number of live adhered cells counted by flow cytometry (see the "Methods" section). MSCs were seeded at a low density (~ 25 cells/mm²) to avoid potential effects from cell–cell interactions (Figure S1C). On elastic alginate hydrogels with 0.8 mM RGD, MSCs secreted significantly more particles on the soft hydrogel (~ 20 000

particles/cell) than on the stiff hydrogel (~ 10 000 particles/cell), while MSCs on a plastic substrate secreted 5 times fewer particles (~ 4000 particles/cell) than MSCs on the soft hydrogel (Figure 1B, i). MSCs remain rounded on the soft hydrogel, while they show increased cell spreading and decreased circularity as the substrate becomes rigid (Figure S1D), suggesting that changes in EV secretion per cell as a function of substrate elasticity are associated with cell shape. Analysis of the particles pelleted after the 10 000g centrifugation showed a lower number per cell, and the number did not depend on substrate elasticity (Figure S2A). Thus, we focused on the EVs remaining in the supernatant after the 10 000g centrifugation. For these EVs, the particle size distribution remained similar across different substrates with median diameter ~ 120 nm (Figure 1B, ii and iii). Analysis of particle preparations by transmission electron microscopy (Figures 1C, i, and S2B) showed that membrane-bound vesicles exhibit mean diameter ~ 70 nm (Figure 1C, ii) and circularity ~ 0.75 (Figure 1C, iii) regardless of substrates. Moreover, EVs from different substrates expressed similar levels of late endosomal markers CD63 and CD9^{1–3} (Figure 1D). Importantly, levels of rRNA (rRNA) in particle preparations were similar across hydrogels or plastic substrates, and rRNA as a percentage of total RNA was lower than that found in untreated MSCs or particles derived from H₂O₂-treated apoptotic MSCs (Figure S2C), ruling out apoptosis as a potential factor of increased EV secretion on the soft hydrogel. MSCs showed a similar level of EV secretion on faster stress-relaxing alginate-RGD hydrogels as elastic hydrogels (Figure S3A), suggesting that stress relaxation times of hydrogels do not impact EV secretion. The effect of substrate elasticity on EV secretion was also observed for primary mouse bone marrow MSCs and clonally derived D1 mouse MSCs²⁸ (Figure S3B), as well as on RGD-bearing polyethylene glycol-diacrylate (PEG-DA) hydrogels (Figure S3C) with similar mechanical properties to elastic

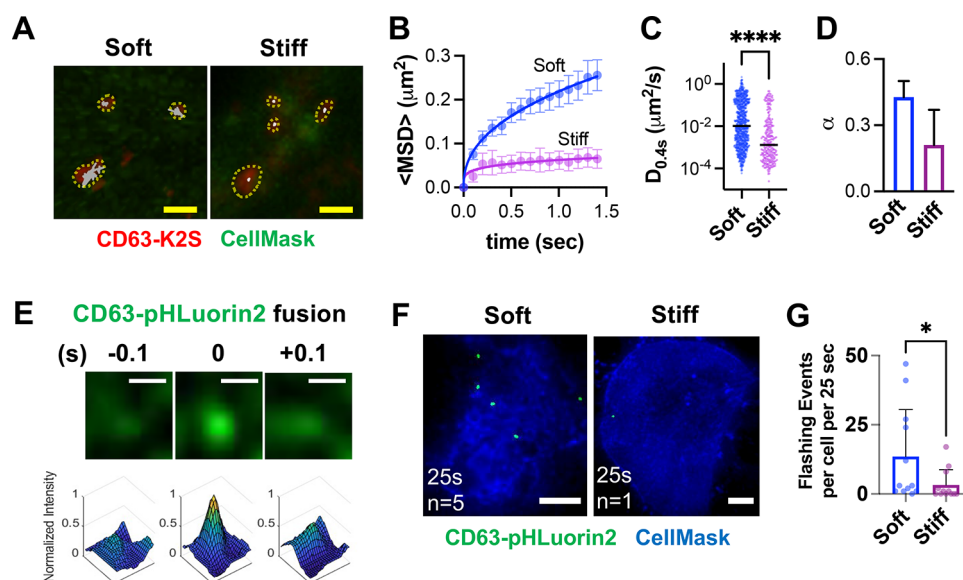


Figure 3. Softer hydrogel substrates facilitate intracellular MVB trafficking and fusion with the plasma membrane. (A) Representative TIRF images of CD63-K2S⁺ MVBs in D1 mouse MSCs and their full 2D MSD tracks under tested conditions. Yellow circles indicate tracked CD63-K2S⁺ MVB regions. Scale bar = 0.5 μm . (B) Ensemble $\langle\text{MSD}\rangle$ vs time plots. Data are fit to eq 1. (C) Values of $D_{0.4s}$ for tracks. *, $p < 0.0001$, via unpaired Mann–Whitney test. (D) Values of exponent α for curves in (B). (E) Top: representative image of event within a cell adhered for 24 h on the soft hydrogel. Scale bar = 0.5 μm . Bottom: plot of normalized fluorescence intensity for images; x – y axes represent image pixels. (F) Representative TIRF images of CD63-pHLuorin2⁺ D1 mouse MSCs for tested conditions. Cumulative events (n) up until the indicated time (sec) are projected on the image. Scale bars = 5 μm . (G) Number of MVB fusion events per cell is significantly increased for MSCs on soft vs stiff hydrogels ($N = 12$ cells per condition). *, $p < 0.05$, via unpaired Mann–Whitney test. For (B–D), tracks N are Soft, 989 tracks; Stiff, 282 tracks. Tracks for all conditions were obtained from $N = 12$ cells each. Error bars denote the 95% confidence interval (CI) for (B) and (D) and the standard deviation (SD) for (G).

alginate hydrogels (Figure S3D). Thus, substrate elasticity is an important determinant of EV secretion from MSCs without affecting vesicle size, morphology, or surface protein expression.

Inhibition of Outside-In Integrin–Ligand Interaction Promotes EV Secretion. We next evaluated the role of integrin-mediated cell adhesions on EV secretion for cells on hydrogel substrates. The binding of talin to the cytoplasmic domain of integrin β_3 activates integrin inside-out signaling, while ligand binding induces outside-in signaling via focal adhesion kinase (FAK)²⁹ (Figure 2A). To test roles of talin and FAK in EV secretion, we treated human MSCs on elastic alginate-RGD hydrogels with siRNA against talin or FAK over 3 days followed by evaluation of EV secretion. The knockdown efficiency of talin and FAK was ~80% (Figure S4A). While knockdown of talin expression had no effect, knockdown of FAK significantly increased EV secretion per cell on the stiff hydrogel (Figure 2B). These results support the notion that integrin–ligand-mediated focal adhesions limit EV secretion, which is enhanced on soft hydrogels (Figure 1B) where focal adhesions are less developed.³⁰

We sought to understand whether changes in integrin–ligand interactions on substrates are sufficient to influence EV secretion. When human MSCs were plated on elastic alginate-RGD hydrogels in the presence of 3 μM Mn^{2+} , a treatment known to increase integrin–ligand affinity,³¹ EV secretion was decreased to a greater extent on the soft hydrogel than the stiff hydrogel (Figure 2C). In contrast, treatment of MSCs with cilengitide, which interfere with integrin binding to RGD,³² significantly increased EV secretion on both soft and stiff hydrogels (Figure 2D). Neither treatment significantly affected the number of cells seeded on hydrogels (Figure S4B) or

particle size (Figure S4C). Consistent with these results, decreasing the RGD concentration from 0.8 to 0.16 mM increased EV secretion per cell by ~2-fold on both soft and stiff hydrogels (Figure 2E), while it also maintained the number of adhered cells per substrate (Figure S4D) and particle size (Figure S4E). Thus, minimizing integrin–ligand interactions promotes EV secretion.

Softer Substrates Facilitate Intracellular MVB Trafficking and Fusion with the Plasma Membrane. To further understand how cell–matrix interactions mediate nanoscale events that result in EV secretion from MSCs, we tested the effect of substrate elasticity on intracellular trafficking of CD63⁺ MVBs. To visualize CD63⁺ MVBs within cells, we fused the red fluorescent protein Katushka2S (K2S) to CD63 and transduced CD63-K2S into D1 mouse MSCs as described.³³ We imaged CD63-K2S⁺ MSCs on soft or stiff PEG-DA hydrogels with 0.8 mM RGD using total internal reflection fluorescence (TIRF) microscopy in order to quantify intracellular transport³⁴ (Figure 3A, Videos S1 and S2). Tracked MVB size was not significantly different across tested conditions (Figure S5A). CD63-K2S⁺ MVBs were tracked by calculating their ensemble-averaged mean squared displacement (MSD) over time (t). Data were collected every $\Delta t = 0.1$ s and fit to the transport equation:

$$\langle\text{MSD}\rangle = K_{\alpha} t^{\alpha} \quad (1)$$

with K_{α} as the transport coefficient and α as the transport exponent.³³ The transport exponent α is ~1 for Brownian motion when particle transport is unimpeded, and <1 for subdiffusive, or impeded, transport. We also calculated the two-dimensional effective diffusion coefficient D_{τ} of tracks:

$$D_{\tau} = \text{MSD}(\tau)/4\tau \quad (2)$$

Track D_{τ} were calculated over each time interval $\tau = 4\Delta t = 0.4$ s as

$$D_{0.4s} = \text{MSD}(\tau = 0.4 \text{ s}) / 4(0.4 \text{ s}) \quad (3)$$

CD63-K2S⁺ MVBs in MSCs transported more rapidly on the soft hydrogel than the stiff hydrogel as indicated by $\langle \text{MSD} \rangle$ versus t plots (Figure 3B) and diffusion coefficient $D_{0.4s}$ (Figure 3C). The transport exponent α across all the conditions was less than 1 (Figure 3D), suggesting that MVB transport is impeded by cytoplasmic contents; exponent α showed a decrease on the stiff hydrogel. Sorting tracks into “slow” or “fast” subgroups reveals that more tracks are considered “slow” for cells on the stiff hydrogel (Figure S5B). Thus, softer substrates facilitate intracellular MVB transport.

We next evaluated the impact of cell–matrix interactions on the fusion of MVBs with the plasma membrane, an event that results in exosome secretion.^{1,2} To accomplish this, we fused the pH-sensitive reporter pHluorin2 to CD63 as described.⁷ This reporter will turn on GFP fluorescence when pH changes from low (acidic) to high (neutral) as occurs when acidic CD63⁺ MVBs carrying exosomes fuse with the plasma membrane and release exosomes into the pH-neutral extracellular space. After transducing CD63-pHLuorin2 into D1 mouse MSCs, we imaged MSCs seeded on soft or stiff PEG-DA hydrogels with 0.8 mM RGD over time using the same TIRF microscopy method every $\Delta t = 0.1$ s with total time $T = 25$ s. Flashing events were determined using a custom program (see the “Methods” section). The intensity for counted events exhibited a sharp increase followed by a rapid decrease (Figure 3E); substrate elasticity does not impact the kinetics of flashing events (Figure S5C). MSCs on the stiff hydrogel produced significantly less events than MSCs on the soft hydrogel (Figure 3F,G, Videos S3 and S4). Thus, softer hydrogels promote nanoscale biological events that result in increased EV secretion.

Arp2/3 Limits Intracellular MVB Trafficking in MSCs on Substrates. We sought to understand mechanisms behind how biophysical regulation of cell–matrix interactions impacts EV secretion. Because myosin-II contractility is known to mediate mechanosensing, we tested whether its inhibition would rescue EV secretion from MSCs on stiff substrates. Surprisingly, 50 μM blebbistatin, an inhibitor of myosin-II ATPase, did not impact exosome secretion from human MSCs on either soft or stiff elastic alginate-RGD hydrogels (Figure S6A). Thus, substrate-stiffness-mediated changes in EV secretion do not require myosin-II activity. The average mesh size of intracellular cytoskeleton networks in mesenchymal cell types is typically ~ 50 nm³⁵ for cells cultured on plastic; hence, the mesh likely impedes the transport of MVBs (Figure 3A–D) that contain multiple ILVs, which are released as exosomes.^{1,2} Since cells on softer substrates show more fluidlike, less dense actin cytoskeletons,³⁶ which can be regulated independently of myosin-II,³⁷ we investigated the role of actin networks in EV secretion from MSCs on substrates. FAK is known to promote actin assembly by interacting with the actin related protein 2/3 (Arp2/3) complex,³⁸ and inhibition of FAK rescues EV secretion on the stiff hydrogel (Figure 2B). We sought to inhibit Arp2/3 in MSCs as they were just beginning to undergo cell spreading and form actin networks. Thus, we first confirmed that MSCs seeded on substrates for a shorter period of time (~ 4 h) followed by washing and EV collection after 24 h show a

similar difference in EV number per cell between soft and stiff hydrogels (Figure S6B). Treatment of human MSCs with 5 μM CK869, an Arp2/3 inhibitor, increased EV secretion on the stiff hydrogel, and the effect was also observed on the soft hydrogel to a lesser but significant extent (Figure 4A). Arp2/3

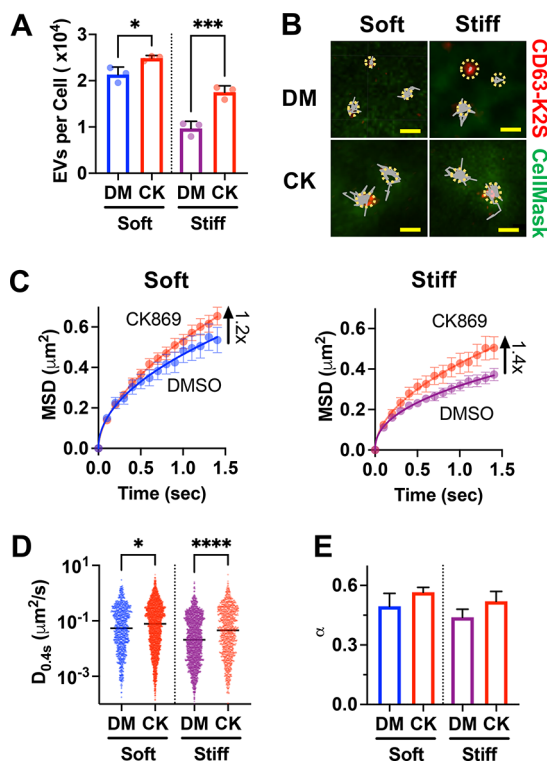


Figure 4. Arp2/3 limits EV secretion from MSCs on hydrogels by inhibiting MVB transport. (A) Primary human MSCs treated with 5 μM CK869 (Arp2/3 inhibitor, CK) exhibit significantly increased EV secretion compared to DMSO (DM). $N = 3$ experiments. *, $p < 0.05$; ***, $p < 0.001$, via one-way ANOVA with Tukey's post-test. (B) Representative TIRF images of CD63-K2S⁺ MVBs in D1 mouse MSCs and their full 2D MSD tracks. Yellow circles indicate tracked CD63-K2S⁺ MVB regions. Scale bar = 0.5 μm . (C) Ensemble $\langle \text{MSD} \rangle$ vs time plots. Data were fit to eq 1. (D) Values of $D_{0.4s}$ for tracks. *, $p < 0.05$; ****, $p < 0.0001$, via Kruskal–Wallis test with Dunn's post-test. (E) Values of exponent α for curves in (C). For (C–E), track N are Soft (DM), 960 tracks; Soft (CK), 2921 tracks; Stiff (DM), 1991 tracks; and Stiff (CK), 1182 tracks. Error bars denote SD for (A) and 95% CI for (C) and (E).

inhibition did not change the size of tracked CD63-K2S⁺ MVBs in MSCs on substrates (Figure S6C). However, Arp2/3 inhibition significantly enhanced transport on either substrate as indicated by representative tracks (Figure 4B, Videos S5, S6, S7, and S8), $\langle \text{MSD} \rangle$ versus t plots (Figure 4D), and $D_{0.4s}$ (Figure 4E), while transport exponent α remained unchanged at ~ 0.5 (Figure 4F). Thus, Arp2/3 limits MVB transport and EV secretion on hydrogels.

We next characterized changes in actin cytoskeleton structural organization associated with substrate-elasticity-directed EV secretion. Confocal imaging analysis shows that mean intensity of phalloidin-Alexa488-labeled F-actin signal per cell is increased in MSCs on the stiff hydrogel after cell adhesion for 4 h, while Arp2/3 inhibition by CK869 for 2 h is sufficient to decrease the signal intensity on both substrates (Figure 5A). To further understand changes in nanoscale F-

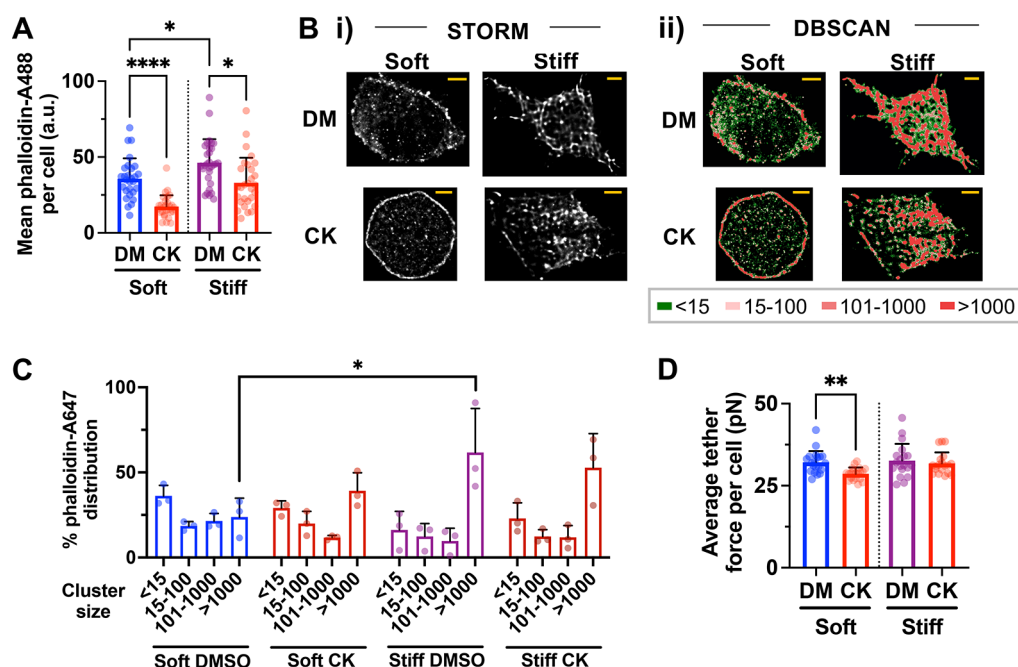


Figure 5. Nanoscale organization of actin cytoskeleton in MSCs on hydrogel substrates. (A) Mean intensity of phalloidin-Alexa488 (A488) signals in MSCs as a function of substrate elasticity in the presence of DMSO (DM) or 5 μ M CK869 (CK). *, $p < 0.05$; ****, $p < 0.0001$, via Welch's one-way ANOVA with Dunnett's T3 post-test. $N = 28$ –30 cells for each group. (B) Representative images from MSCs labeled with phalloidin Alexa647 (A647) under different conditions using (i) STORM visualized via normalized integrated Gaussian distribution and (ii) DBSCAN analysis of STORM localizations. The color bars in DBSCAN analysis denote the number of phalloidin-A647 localizations per cluster. Scale bar = 3 μ m. (C) Quantification of phalloidin-A647 localization distribution in different clusters per cell from DBSCAN analysis. *, $p < 0.05$, via two-way ANOVA with Tukey's post-test. $N = 3$ cells for each group. (D) Measurement of average membrane tether force per cell by AFM. **, $p < 0.01$, via Welch's one-way ANOVA with Dunnett's T3 post-test. $N = 20$ cells for each group. For all, error bars denote SD.

actin organization, we performed super-resolution direct Stochastic Optical Reconstruction Microscopy (dSTORM)^{39,40} imaging using TIRF microscopy, revealing molecular localizations of phalloidin-Alexa647-labeled F-actin signal at the interface between the cell and substrate (Figure 5B, i) with super-resolution precision (~ 40 nm average localization accuracy) (see the “Methods” section). The density-based spatial clustering of applications with noise (DBSCAN) algorithm was then used to determine whether F-actin clusters are present as shorter fragments (<15 localizations per cluster), which were previously observed in red blood cells,⁴¹ or more substantial fibers (>1000 localizations per cluster) (Figure 5B, ii). Both shorter fragments and fiber F-actin signals were observed when MSCs were seeded on the soft hydrogel, while fibers were more prominent on the stiff hydrogel (Figure 5C). CK869 treatment for 2 h did not alter the distribution of different F-actin clusters on both substrates, suggesting that Arp2/3 mediates the amount of actin polymers per cell, but not actin clustering or bundling within this time scale. A biophysical factor that can also potentially limit MVB fusion and exosome release is the membrane-cytoskeleton attachment (MCA), which is known to regulate both exocytosis and endocytosis.⁴² The MCA can be quantified by the measurement of force for membrane tether formation using atomic force microscopy (AFM)^{43–45} (see Methods). Our results show that substrate elasticity does not impact the force of membrane tether formation within 4 h of cell adhesion, although CK869 treatment for 2 h slightly decreases tethering on the soft hydrogel (Figure 5D). Together, the

presence of larger actin fibers near the cell surface likely impedes MVB transport and fusion within cells on hydrogels.

MSC EVs from Different Substrates Retain Therapeutic Activity and Cargo Contents against Acute Lung Injury *In Vivo*. Our results collectively show that the combination of a soft ($E \sim 3$ kPa) hydrogel substrate (Figure 1B) and a lower (0.16 mM) RGD concentration (Figure 2E) results in a total ~ 10 -fold increase in EV secretion per cell relative to that in plastic culture. Thus, we sought to evaluate the potential impact of substrate elasticity on EV content and functionality. MSC-derived EVs are known to attenuate acute lung injury.^{46,47} Thus, we intratracheally (i.t.) delivered a matched dose of EVs (6×10^7 per 20 g of mouse) from primary mouse MSCs cultured on soft or stiff PEG-DA hydrogels with 0.16 mM RGD or plastic culture 4 h after inducing lung injury in mice using lipopolysaccharides (LPS) (Figure 6A). After 24 h, a significant reduction in lung edema (Figure 6B, i) and vascular permeability as shown by albumin accumulation in lung parenchyma (Figure 6B, ii) were observed for mice treated with EVs from all tested substrates. At this dose, EVs from MSCs on the soft hydrogel facilitate the reduction of edema and vascular permeability in LPS-treated mice to a greater extent than EVs from MSCs on plastic (Figure 6B). The therapeutic mechanism by which MSC-derived EVs attenuate acute lung injury is reported to require presentation of the CD44 receptor on the EV surface, which is known to facilitate uptake into host monocytes, monocyte-derived macrophages, and alveolar type II cells.¹⁴ Thus, we sought to test the possibility of whether EVs derived from cells on different substrates provide therapeutic efficacy through a

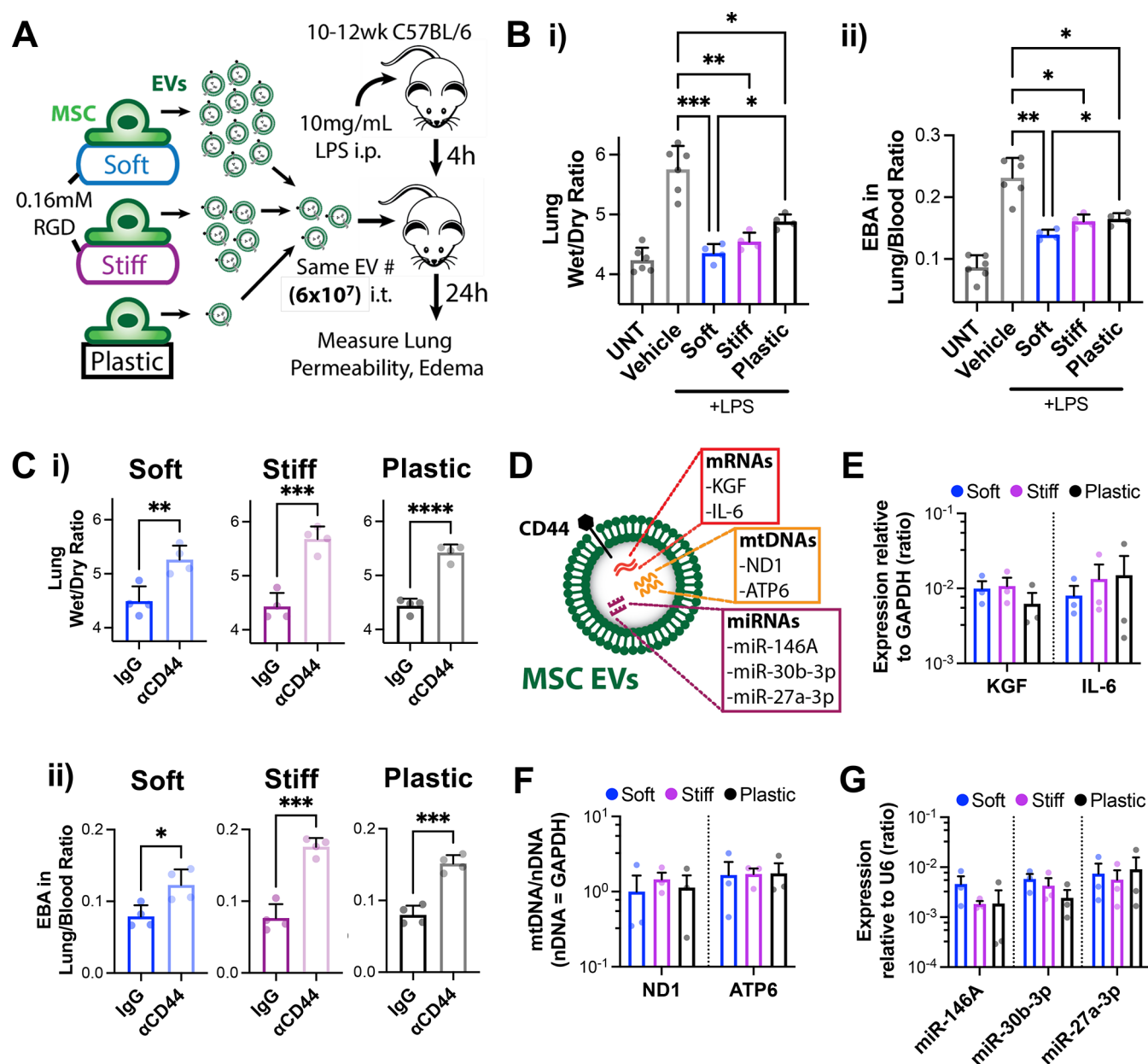


Figure 6. Substrate elasticity does not compromise the efficacy or cargo contents of MSC-derived EVs to resolve acute lung injury. (A) Overview of strategy to determine EV therapeutic efficacy in a preclinical model of acute lung injury. EVs were collected after plating primary mouse MSCs on indicated substrates for 4 h followed by 24 h in culture. EVs (6×10^7 per 20 g of mouse) from each group were administered intratracheally (i.t.) 4 h after intraperitoneal (i.p.) injection of lipopolysaccharides (LPS). (B) Measurements of (i) lung edema by quantifying lung wet–dry ratio and (ii) lung vascular permeability by quantifying Evans blue albumin (EBA) accumulation. *, $p < 0.05$; **, $p < 0.01$; ***, $p < 0.001$, via Welch's one-way ANOVA with Dunnett's T3 post-test. $N = 6$ mice for untreated and LPS + vehicle groups; $N = 4$ mice for experimental groups. (C) CD44 blocking antibody reverses efficacy of EVs (3×10^8 per 20 g of mouse) from different substrates. (i) Lung edema measurements. (ii) Lung vascular permeability measurements. *, $p < 0.05$; **, $p < 0.01$; ***, $p < 0.001$; ****, $p < 0.0001$, via unpaired t test. $N = 4$ mice per group. (D) Overview of cargo contents within EVs known to affect therapeutic outcomes. (E) Expression of mRNAs in EVs known to affect lung injury outcomes, measured by qPCR. (F) Presence of mtDNA (normalized to nDNA) in EVs, measured by qPCR. (G) Presence of miRNAs (normalized to U6 RNA) in EVs known to affect lung injury outcomes, measured by qPCR. For (E–G), data represent the mean of $N = 3$ experiments each with $N = 3$ qPCR reactions per condition. Error bars denote SD for (B–C) and SEM for (E–G).

similar mechanism that requires uptake by host cells through presence of free CD44 receptor on the EV surface. To accomplish this, we treated the maximum effective dose of EVs (3×10^8 per 20 g of mouse) secreted from MSCs on different substrates with a CD44 blocking antibody, all of which negated their therapeutic activity in terms of lung edema and permeability (Figure 6C), demonstrating that MSC-derived

EVs from different substrates leverage CD44 to achieve therapeutic efficacy in acute lung injury. We also profiled EV cargo composition from primary mouse MSCs in terms of different molecules known to be essential in ameliorating acute lung injury (Figure 6D). EVs from different substrates showed a similar level of keratinocyte growth factor (KGF)¹³ and interleukin-6 (IL-6)⁴⁸ RNAs (Figure 6E), mitochondrial

DNAs¹⁷ (Figure 6F), and miRNAs^{49–51} (Figure 6G). Thus, soft hydrogels enhance EV secretion without compromising functionality or cargo contents to resolve injury.

CONCLUSIONS

The results presented here establish a fundamental nanoscale relationship between functional EV secretion and cell–matrix interactions in the microenvironment. Cells on softer substrates produce more EVs than cells on stiffer substrates. Despite the difference in the number of EVs released, EVs remain similar in terms of their size, morphology, and expression of late endosomal markers. As cells adhere to substrates, integrins become increasingly activated, leading to a decrease in EV production. Mechanistically, soft substrates promote EV secretion by enhancing intracellular MVB transport and fusion to the plasma membrane, while FAK and Arp2/3 limit EV secretion (Figure 7). Although EV secretion is increased by cells on softer hydrogel substrates, EVs retain similar cargo contents and efficacy in a mouse model of acute lung injury.

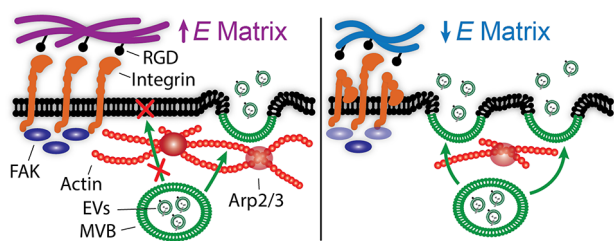


Figure 7. Summary of nanoscale events regulating EV secretion by cell–matrix interactions. Softer substrates decrease outside-in integrin activation, focal adhesions, and Arp2/3-mediated actin network formation, facilitating the ability of MVBs to transport and fuse with the plasma membrane to release EVs.

Cells localized within various environments likely exhibit distinct functions based on properties of each environment. Our study suggests the possibility that softer environments typical of vascular regions might be naturally designed for cells to secrete more EVs, which can then travel over longer distances via circulation. The effect of cell–matrix interactions on small EV populations can be further characterized by taking heterogeneity into consideration, including exosomes and nonexosomal vesicles.⁵² Although the 3D density of MVBs in MSCs has yet to be studied, a recent study used focused ion beam milling and scanning electron microscopy to profile the density of MVBs in a neural tissue and reported ~ 0.2 MVBs per μm^3 .³⁵³ Other studies have used electron microscopy to perform a 3D profiling of ILVs within reported in a range from 50 to 100 ILVs per MVB.^{54,55} Given that the volume of a cell⁵⁶ is $\sim 3000\text{--}6000\ \mu\text{m}^3$, estimates based on the above recent studies suggest a total pool of 0.3 to 2.0×10^6 ILVs is released. Thus, our results suggest that a fraction of EVs is released from cells at a given time, the process that is subject to regulation by cell–matrix interactions.

Cells contain a dense cytoplasm that is considered a viscous semisolid. It was shown that nanoparticle transport in cells is hindered as the actin mesh becomes denser, resulting in subdiffusion.⁵⁷ Consistent with previous results,³⁶ our study shows that cells on stiffer substrates spread more and develop a denser actin mesh at nanoscale. In this context, our results suggest that CD63⁺ MVBs are likely constrained by this denser

mesh within cells spreading on stiffer substrates. If MVBs are unable to transport freely, then it follows that they are less readily able to reach the plasma membrane to undergo fusion and release EVs as demonstrated here. The approach utilized here can also be extended to study the role of extrinsic material properties,⁵⁸ such as substrate dimensionality and geometry, as well as dynamically tunable hydrogels⁵⁹ in functional EV secretion.

Translation of EVs as treatments against tissue injuries will require efficient and scalable production of EVs *ex vivo*. Currently, limitations exist on the number of EVs that can be produced for clinical studies, especially if studies require autologous EVs.⁶⁰ In addition, potential donor-to-donor variability of allogeneic EVs could negatively impact the reproducibility of therapeutic outcomes.⁶¹ Hence, there is a need for maximizing the yield of therapeutic EVs from a single donor source on a per cell basis. In fact, maximizing the number of therapeutic EVs produced per cell by optimizing cell culture conditions is predicted to be the single most important driver of feasibility for producing EVs at large scales necessary for clinical translation.⁶² Thus, producing more EVs per cell in a given process will lead to a significant increase in clinical trial throughput, given that EVs maintain a similar therapeutic efficacy. Previous efforts to improve EV productivity include small molecules,⁶³ membranes or fibers,⁶⁴ hollow-fiber bioreactors,⁶⁵ and nanoporation,⁶⁶ but further studies are warranted to determine whether or not increased EV production occurs at the expense of therapeutic efficacy *in vivo*. In contrast to these approaches, hydrogels with tunable properties provide the advantage of recapitulating salient physiological features of microenvironments from which cells are derived. From a practical perspective, tunable hydrogels can be useful as a module to be integrated with other approaches, such as microfluidic-based bioreactors to improve the manufacturing process of functional EVs. Our study shows that tuning of matrix properties alone is sufficient to increase the number of EVs produced per cell, while retaining the cargo contents and a CD44-mediated mechanism of action known to be essential for the resolution of acute lung injury. Intriguingly, a softer substrate also decreases the effective dose of EVs to achieve therapeutic efficacy in this context. This result suggests the possibility that there is a set of cargo molecules that may become packaged into EVs when a substrate becomes softer; thus, broader molecular profiling with functional validation studies will help elucidate this possibility. In addition, it is possible that softer substrates facilitate the production of a distinct EV subpopulation, which could contribute to therapeutic efficacy. Sub-fractionation techniques, such as high-density gradient centrifugation⁵² and asymmetric-flow field-flow fractionation,⁶⁷ can be used to understand the impact of cell–matrix interactions on the production of EV subpopulations.

In summary, this study describes the importance of cell–matrix interactions in regulating EV secretion at the nanoscale and suggests considerations for fundamental mechanisms of EV biogenesis in microenvironments and biomaterial-based strategies to control the production of EVs as nanotherapeutics for tissue injuries.

METHODS

Material Preparation and Hydrogel Formation. Raw sodium alginates with different molecular weights, low (10/60, ~ 120 kDa) and high (Manugel, ~ 240 kDa), were obtained from FMC

Corporation. Alginate was purified through dialysis in a 3.5 kDa membrane submerged in water, followed by treatment with activated charcoal (Sigma) 0.5 g per 1 g of alginate. It was then filtered, frozen, and lyophilized to obtain a solid polymer. Conjugation of RGD (amino acid sequence GGGGRGDSP, Peptide 2.0) to alginate polymers was performed using a method involving carbodiimide chemistry as described previously^{22–24} at DS10 (0.8 μ M) or DS2 (0.16 μ M). Physically cross-linked hydrogels were formed by mixing 1% Manugel and 1% 10/60 (2% total), adding the mixture to a syringe, and locking it to another syringe with CaSO₄ (Sigma) to achieve final calcium concentrations of 10 mM (softer) and 25 mM (stiffer).³³ After mixing, the solutions were deposited under glass for 2 h to form a hydrogel. Covalently cross-linked hydrogels were formed using carbodiimide chemistry and adipic acid dihydrazide (AAD, Sigma) as described.²⁶ Alginate solution (1% Manugel and 1% 10/60) was mixed with 4.8 mg/mL hydroxybenzotriazole (Sigma), 50 mg/mL 1-ethyl-3-(3-(dimethylamino)propyl)carbodiimide (Sigma), and either 1.5 mM (soft) or 6 mM (stiff) AAD. Solutions were incubated under glass for 12–18 h to form a hydrogel. PEG-DA hydrogels were formed by adding the materials: 10 mM sodium L-ascorbate (Sigma), 4 mM tris(2-carboxyethyl)phosphine (Sigma), 1× phosphate-buffered saline (PBS), 0.8 or 0.16 mM cys-RGD peptide (sequence CGGGGRGDSP, Peptide 2.0), PEG-DA Mn 700 (Sigma), and lithium phenyl(2,4,6-trimethylbenzoyl)phosphine (TCI Chemicals) in varying concentrations to achieve desired range in mechanical properties upon 365 nm ultraviolet light exposure.

Mechanical Characterization of Hydrogels. The mechanical properties of hydrogels or tissues were obtained using rheometry via Netzsch Kinexus as described.³³ Storage (G') and loss (G'') moduli were measured through a frequency sweep by lowering the 8 mm plate geometry to a 5% normal strain followed by a rotation that induced a 0.5% shear strain at an increasing frequency and finally measurement of the resulting shear stress. The complex shear modulus G^* was calculated:

$$G^* = \sqrt{G'^2 + G''^2} \quad (4)$$

Young's Modulus (E) was calculated with the equation:

$$E = 2G^*(1 + \nu) \quad (5)$$

using the value of G^* obtained at 1 Hz, with Poisson's ratio $\nu = 0.5$. To determine stress relaxation, the geometry was lowered at constant velocity (25 μ m s⁻¹) through the linear elastic region until a 15% strain was reached, followed by measurement of normal force over time.

Cell Culture. Cells were cultured at 37 °C in 5% CO₂. Human MSCs (hMSCs) were derived by plastic adherence of mononucleated cells from human bone marrow aspirate (Lonza). After 3 days, adherent cells were cultured in the hMSC medium: α -minimal essential medium (α MEM, Thermo) supplemented with 20% fetal bovine serum (FBS, Atlanta Biologicals), 1% penicillin/streptomycin (P/S, Thermo Fisher Scientific), and 1% GlutaMAX (Thermo). After reaching 70–80% confluence at 10–14 days, cells were split, expanded in hMSC medium, and used at passage 3. D1 MSC cells (CRL-12424, ATCC) were cultured using high-glucose DMEM (Thermo) supplemented with 10% FBS, 1% P/S (Thermo), and 1% GlutaMAX (Thermo) to 80% confluency before passaging, no more than 30 times. Cells were routinely tested for mycoplasma contamination and only used if no contamination was present.

Cell Seeding on Hydrogels. Hydrogel discs were placed in ultralow binding polystyrene well plates (Corning) to ensure cells attach to hydrogels and not the plate surface. Hydrogels were washed with Hank's buffered salt solution (HBSS, Thermo) for at least 3 days before seeding cells. Cells were seeded at a low density (25 cells/mm²). After seeding, hydrogels were washed thoroughly to remove unattached cells. Drug treatments of 3 μ M MnCl₂ (Fisher Scientific), 200 nM cilgintide (Cayman) and 5 μ M CK869 (Cayman) were applied during and after cell adhesion to substrates. To evaluate the number of live cells seeded on the substrate, cells were detached by incubating with Accutase Cell Detachment Solution (Innovative Cell

Technologies, Inc.) for 10 min at 37 °C. Cells were then washed by centrifugation and directly added to HBSS containing calcein AM (1:2000; Biotium), ethidium bromide (1:2000; Thermo Fisher Scientific), and a predefined number of allophycocyanin (APC) beads (BD). After incubation at room temperature for 10 min, the samples were analyzed for live and dead cell number by flow cytometry.

Cell Morphology Analysis on Hydrogels. To evaluate cell morphology on substrates, cells were washed with HBSS, incubated with calcein AM (1:2000) for 10 min at 37 °C, and imaged using a Nikon Eclipse Ts2R inverted fluorescence microscope. Cell circularity was calculated with the equation:

$$\text{Circularity} = \frac{4\pi(\text{Area})}{\text{Perimeter}^2} \quad (6)$$

Particle Size and Number Characterization. Particle size and number were obtained using Nanoparticle Tracking Analysis 3.2 (NTA) via NanoSight NS300 (Malvern) using a 405 nm laser. Samples were introduced by syringe pump at a rate 100 μ L/min. Three 30 s videos were acquired using camera level 14 followed by detection threshold 7. Camera focus, shutter, blur, minimum track length, minimum expected particle size, and maximum jump length were set automatically by the software. Samples were diluted as needed to maintain particles per video from 100 to 2000. To ensure specificity, all samples were tested as compared to appropriate blank conditions.

Transmission Electron Microscopy. Samples were prepared by placing 10 μ L onto a 300-mesh copper grid with carbon-coated Formvar film (Electron Microscopy Sciences) and incubated for 2 min. Excess liquid was removed by blotting. Grids were placed briefly on 10 μ L of 2% uranyl acetate, followed by blotting to remove excess liquid, and placed again. Grids were examined via JEOL JEM-1400F transmission electron microscope, operating at 80 kV. Digital micrographs were acquired using an AMT NanoSprint1200-S CMOS Camera and AMT software (Version 701). Particle diameter and sphericity were determined manually from images using ImageJ. The circularity of particles was defined by eq 6.

Characterization of Late Endosomal Proteins in EVs. CD63 and CD9 expression was determined using in-house ELISA assays. Capture antibodies (CD63: BioLegend, 353014; CD9: BioLegend, 312102) were adhered to Nunc MaxiSorp flat-bottomed coated plates (Invitrogen, 44–2404–21) overnight followed by blocking for 1 h with 1% bovine serum albumin (Roche) in PBS. After washing, samples were incubated overnight followed by incubation with biotin-conjugated detection antibodies (CD63: GeneTex, GTX52381; CD9: Miltenyi, 130–103–989), Streptavidin-HRP (R&D Systems), and ELISA substrate (R&D Systems). Reactions were quenched with 1 M HCl, and the absorbance was read at 450 nm. Recombinant protein standards (Sino Biological) were used as comparisons for protein content.

siRNA Transfection. Scrambled siRNA (Dharmacon, D-001810–01–05) or siRNA against FAK (Ambion, 4427038) or TLN1 (Dharmacon, J-012949–05–0002) was diluted to 160 nM in unsupplemented Opti-MEM medium (Thermo) and combined 1:1 with Opti-MEM supplemented with 2% Lipofectamine RNAiMAX (Thermo) and incubated at room temperature for at least 20 min. Cells were washed with HBSS, and fresh growth medium was added to cells. The transfection solution was added dropwise for a final siRNA concentration of 4 nM to treat cells on hydrogels for 3 days followed by EV collection and measurement.

EV Isolation and Preparation. To isolate EVs from cells for cargo characterization and animal experiments, the cells were washed twice with HBSS followed by incubation with serum-free growth medium for 30 min. Afterward, the medium was exchanged with fresh serum-free medium. After the times as indicated in the manuscript, the medium was centrifuged at 2000g for 10 min to remove cell debris followed by centrifugation at 10 000g to remove microvesicles (>500 nm).²⁷ Afterward, the supernatant was added slowly to a 14 mL polystyrene ultracentrifuge tube (Beckman) containing 1.5 mL of 30% sucrose (Fisher Scientific) in PBS and centrifuged at 100 000g for 90

min. The upper nonsucrose layer was aspirated and washed with PBS followed by centrifugation at 100 000g for 90 min. The pellet was resuspended and confirmed to contain concentrated particles measured by NanoSight NS300 (Malvern).

EV Content Characterization. Before extraction, for all samples, particles were incubated with DNase I (Thermo) to remove potential exogenous DNA not contained within particles. DNA samples were treated with RNase A (Qiagen) to remove RNA contaminants, and DNA was extracted using the DNeasy Blood and Tissue kit (Qiagen) followed by qPCR analysis. Total RNA was extracted from samples using the RNeasy Mini kit (Qiagen). Complementary DNA was reverse-transcribed from RNA by SuperScript-III (Thermo Fisher Scientific). For both mRNA and miRNA, a random hexamer primer (Invitrogen) was used. For miRNA, an additional stem-loop RT (SLRT) primer was included at 100 nM for each specific miRNA target (see Table S1 for sequences) as described.⁶⁸ Quantitative PCR was performed in the ViiA7 qPCR system with PowerSYBR Green master mix (Applied Biosystems). Samples were analyzed using primer concentrations of 100 nM each with sequences in Table S1; for miRNA, the forward primer corresponds to the miRNA sequence and the reverse primer corresponds to the stem-loop sequence, which is universal for all targets. Relative gene expression was computed by the delta Ct method by comparing Ct values to a reference gene (*GAPDH* or *U6*). See Table S1 for the list of primers used. Samples were compared to a blank to ensure specificity of the assay (data not shown). To analyze rRNA contents, RNA samples were analyzed by Agilent TapeStation 4200, and 18S rRNA was considered as a peak in the range 1000–2000 nucleotides as in Figure S2C.

Lentiviral-Mediated Expression of CD63 Fused with Fluorescent Proteins. Katushka2S was fused with CD63 in a lentiviral expression vector (CD63-K2S vector) and expressed in D1 MSCs as described previously.³³ The sequence for pHLuorin2 was synthesized by GenScript and exchanged with the Katushka2S in the same vector using restriction enzyme cloning. The resulting CD63-pHLuorin2 lentiviral vector was transduced in D1 MSCs in a similar method as the CD63-K2S vector. Cells were selected by treatment with 5 μ g/mL puromycin over 3 days and confirmed to express fluorescent signal versus nontransduced cells.

TIRF Imaging of Cells on Substrates. To covalently bond cross-linked PEG-DA hydrogel to a thin glass surface, acrylate groups were attached to glass coverslips by silanization as described.⁶⁹ A solution of 3% *v/v* 3-(trimethoxysilyl)propyl acrylate (TCI Chemicals) and 5% *v/v* glacial acetic acid (Fisher Scientific) was prepared in methanol. No. 1 coverslips (Ted Pella) were incubated in the reaction solution for 45 min and thoroughly washed with methanol. The silanized coverslips were then rinsed with ethanol and dried. A thin, flat (~ 40 μ m) layer of PEG-DA hydrogel was formed on the coverslips, followed by cell seeding, both as described above. Before imaging, cells were stained with CellMask Green (Thermo) for Katushka2S experiments and CellMask Deep Red (Thermo) for pHLuorin2 experiments for 5 min at 37 °C followed by washing. Coverslip-hydrogels with seeded cells were mounted with immersion oil (Cargille) of refractive index 1.518 for Katushka2S experiments or 1.514 for pHLuorin2 experiments. Samples were imaged with a DeltaVision OMX SR microscope (GE) with an Olympus 60 \times Apo N objective. Dual-channel 512 \times 512 pixel² (41 \times 41 μ m²) images were obtained using the TIRF imaging mode with TIRF angle set at 80–90°. For each cell, 250 images were obtained over 25 s with frequency 100 ms per image.

CD63-Katushka2S Data Analysis. Using the IMARIS “Surfaces” function, a custom tracking algorithm was created. Intracellular bodies were determined using Gaussian smoothing and local background intensity thresholding (with automatically determined thresholds) to detect surfaces followed by tracking their position (x, y) over time (t). To account for noise within images, bodies were discarded if they were constituted by less than 12 pixels (0.0768 μ m²). Tracks could continue if the body was undetectable for a single time point within the track but not for two or more consecutive time points. MVB area was computed for each time t and reported as the mean area across

total track time T . Tracks were then analyzed via a custom MATLAB (R2017b, MathWorks) program. Track MSD was calculated as

$$\text{MSD}(t) = [x(t) - x(t=0)]^2 + [y(t) - y(t=0)]^2 \quad (7)$$

Ensemble-averaged track data were generated by averaging the MSD for each track i at every time t elapsed since the start of tracking:

$$\langle \text{MSD}(t) \rangle = \frac{1}{N} \sum_{i=1}^N \text{MSD}_i(t) \quad (8)$$

where N is number of tracks. For ensemble-averaged tracks, a lower limit of 15 points (1.5 s) and an upper limit of 180 points (18 s) were defined to constrain the tracks considered for analysis, as uneven track sizes can bias the results. Consequently, the ensemble-averaged data are shown only up to the lower limit ($t = 1.5$ sec). Tracks were sorted into “Slow” or “Fast” populations using a threshold $D_{0.4s} = 0.001$ μ m²/sec.

CD63-pHLuorin2 Data Analysis. Flashing events were determined from image sequences using a custom MATLAB program. Potential event regions were determined by subtracting each image from a rolling average of the 5 previous images. The resulting image was converted to a binary image using a threshold of 40% of the mean image intensity. Regions identified after thresholding containing greater than 20 pixels (0.128 μ m²) were considered. The total intensity within each region at the time of the event was then compared to the total intensity in the same region before the event (i.e., 5 images previous). A ratio of these intensities was taken, and the event was counted if the ratio exceeded three.

Sample Preparation for Imaging of F-Actin in Cells on Hydrogels. To prepare samples for F-actin imaging, glass bottom dishes (No 0., 35 mm; MatTek) were silanized, and a thin layer of PEG-DA hydrogel with varied elasticity was formed as described above. After cell seeding on hydrogels and culturing cells in the presence of DMSO or CK869, cells were permeabilized with 0.0015% saponin (Sigma) in a cytoskeleton buffer (10 mM MES, pH 6.0, 150 mM NaCl, 5 mM EGTA, 5 mM glucose, and 5 mM MgCl₂) for 4 min at room temperature. The samples were then washed with the cytoskeleton buffer 3 times and fixed with 4% paraformaldehyde in the cytoskeleton buffer for 20 min at room temperature. After washing 3 times with the cytoskeleton buffer, the samples were reduced in 0.1% sodium borohydride in PBS for 20 min at room temperature. To label F-actin in cells, the samples were stained with phalloidin-Alexa488 (1:1000; Cayman) for confocal imaging and phalloidin-Alexa647 (1:10000; Cayman) for super-resolution imaging in PBS with 3% BSA for 40 min at room temperature. The samples were washed 3 times with PBS prior to imaging.

Confocal Imaging of F-Actin. Images of phalloidin-Alexa 488-labeled cells on hydrogels were acquired by using the Zeiss LSM 770 confocal microscope with the 10 \times Plan-Apochromat objective by acquiring individual slices of the lateral plane at 1 μ m increments along the axial plane with excitation/emission wavelength of 495/515 nm. A mean projection image was created from each confocal stack, and the average intensity of Alexa488 per cell was analyzed with ImageJ (NIH). Each average intensity value was subtracted by the corresponding mean background intensity value from the same field of view.

Super-Resolution Imaging of F-Actin. Super-resolution direct stochastic optical reconstruction microscopy (dSTORM) imaging was performed on a Nikon Ti inverted microscope with a 100 \times (NA 1.49) oil immersion objective in total-internal reflection (TIR) illumination condition with a 65 mW, 640 nm laser, and an Andor IXON3 Ultra DU-897 EMCCD camera and collected in a far-red channel with EM filter 705/72. All dSTORM imaging phalloidin-Alexa647 data sets were acquired using 80% excitation power setting at 10 ms exposure with the same EM gain after room temperature equilibration using NIS-Elements software. STORM buffer conditions used for oxygen scavenging were the same as reported previously.⁴⁰ A total of 50 000 images were recorded for each cell under each condition; after rejecting overly dense/bleached images, approximately 30 000 images were analyzed in each cell/condition for localization detection in

postprocessing using ThunderSTORM (ImageJ), with the following settings in brief: wavelet filtering (B-spline order 3, scale 2); integrated Gaussian fitting (radius: 3 pixels, initial sigma: 1.6 pixels); local maximum with 8-neighborhood; camera pixel size 160 nm. The localizations were then filtered via intensity to remove a majority of high uncertainty localization, followed by drift correction and removal of duplicate points.

Nanoscale Clustering Analysis of F-Actin. The density-based spatial clustering of applications with noise (DBSCAN) algorithm was used to quantify clustering of F-actin localizations in each cell from dSTORM imaging⁷⁰ via a custom Python (3.8) program. The algorithm groups together localizations that are within a radius (ϵ), given a minimum number of localizations to be considered a cluster (ρ). Here, ϵ = half of average localization uncertainty for each cell (17.8 ± 2.0 nm) to achieve a search radius that would enable at least two phalloidin-Alexa647 localizations overlapping each other by the radius. The ρ value was set at 5 to remove any background signal outside the cell boundary. The F-actin clusters were classified and color-coded into 4 groups: (a) 5 or above, less than 15 (shorter fragments), (b) 15 or above, less than 100, (c) 100 or above, less than 1000, (d) 1000 or above (fiberlike structures). The percentage of F-actin localizations that belong to each cluster group per cell was then quantified and used for statistical analysis.

Measurement of Force for Membrane Tether Formation by Atomic Force Microscopy (AFM). Membrane tethering force was measured by using 3D-BIO AFM (Asylum Research, Oxford Instruments) with TR400PSA cantilevers (OTR4; spring constant = 30 pN/nm). Indentation depth for each measurement was 4 μ m with a velocity of 2 μ m/s, and the force curve for each measurement was recorded by the AFM software (AR14). For each cell, 25–50 force curves were analyzed. In force mode, the piezotransducer (PZT) was set to drive the cantilever to approach, touch, make an indentation, and retract over a predefined distance in the optical axis perpendicular to the cell surface. The force curve was generated from the recorded vertical-axis movement of the PZT and the deflection of the cantilever with a known dimension and a spring constant. In the force curve representing the retraction of the cantilever from a cell, a sudden release of force occurred at the rupture of a membrane tether was quantified via a custom MATLAB program.

Animal Model of Acute Lung Injury. All animal procedures were performed in compliance with NIH and institutional guidelines approved by the ethical committee from the University of Illinois at Chicago. Female C57BL/6J mice were purchased from The Jackson Laboratory and housed in the University of Illinois at Chicago Biologic Resources Laboratory. At age 10–12 weeks, mice were treated with 10 mg/kg lipopolysaccharides (LPS, Sigma) via intraperitoneal injection to induce acute lung injury. After 4 h, mice were anesthetized using ketamine/xylazine (50/5 mg/kg), and EVs (6×10^7 per 20g mouse) were administered by single dose intratracheal instillation. One day after LPS administration, mice were evaluated for lung vascular permeability and edema as described previously.⁷¹ Briefly, mice were anesthetized using ketamine/xylazine (50/5 mg/kg) and a solution of Evans blue albumin (20 mg/kg) was applied via retro-orbital intravenous injection. After 20 min, mice were sacrificed and lung tissue was harvested along with a fraction of circulating blood. Right lung tissue was weighed initially (wet weight) and after 24 h of incubation at 65 °C (dry weight) to calculate wet/dry ratio. Left lung tissue was homogenized and Evans blue extracted with formamide. Evans blue content was measured by absorbance at 620 nm and normalized to that present in circulating blood. For CD44 blocking experiments, EVs (3×10^8 per 20 g of mouse) were incubated with 1 μ g/mL of blocking CD44 antibody (BE0039, BioXCell) or IgG control antibody (BioXCell, BE0090) for 30 min at 4 °C prior to administration.

Statistical Evaluation. Statistics were performed as described in figure captions. All statistical analyses were performed using GraphPad Prism version 9.0.0. Unless otherwise noted, statistical comparisons were made from at least three independent experiments by one-way ANOVA followed by Tukey's multiple comparison test when standard deviations did not vary between test groups and by

one-way Welch ANOVA followed by Dunnett T3 multiple comparisons test when standard deviations were variable. For the data sets that do not show normal distributions based on the Anderson–Darling normality test, the Mann–Whitney test was used to compare two groups, and the Kruskal–Wallis test followed by Dunn's multiple comparisons test was used to compare more than two groups. A p -value of less than 0.05 was considered statistically significant.

ASSOCIATED CONTENT

Supporting Information

The Supporting Information is available free of charge at <https://pubs.acs.org/doi/10.1021/acsnano.1c03231>.

Characterization of hydrogel substrate mechanical properties and cell attachment, stiffness-dependent particle properties, and elasticity-dependent EV secretion; investigating roles of integrin–ligand interactions in mediating EV secretion from MSCs seeded on hydrogel substrates; tracking intracellular transport and fusion of MVBs; investigating biophysical mechanisms behind MVB transport and fusion; reverse transcription and quantitative PCR primers (PDF)

Video S1: Tracking data overlaid with imaging data for representative transport of single CD63-K2S⁺ bodies within a cell adhered for 24 h on the soft hydrogel shown in Figure 3A (AVI)

Video S2: Tracking data overlaid with imaging data for representative transport of single CD63-K2S⁺ bodies within a cell adhered for 24 h on the stiff hydrogel shown in Figure 3A (AVI)

Video S3: CD63-pHLourin2 flashing event appearance for a cell adhered for 24 h on soft hydrogel shown in Figure 3F (AVI)

Video S4: CD63-pHLourin2 flashing event appearance for a cell adhered for 24 h on stiff hydrogel shown in Figure 3F (AVI)

Video S5: Tracking data overlaid with imaging data for representative transport of single CD63-K2S⁺ bodies within a cell adhered for 4 h on the soft hydrogel treated with vehicle shown in Figure 4B (AVI)

Video S6: Tracking data overlaid with imaging data for representative transport of a single CD63-K2S⁺ body within a cell adhered for 4 h on the soft hydrogel treated with CK-869 shown in Figure 4B (AVI)

Video S7: Tracking data overlaid with imaging data for representative transport of single CD63-K2S⁺ bodies within a cell adhered for 4 h on the stiff hydrogel treated with vehicle shown in Figure 4B (AVI)

Video S8: Tracking data overlaid with imaging data for representative transport of single CD63-K2S⁺ bodies within a cell adhered for 4 h on the stiff hydrogel treated with CK-869 shown in Figure 4B (AVI)

AUTHOR INFORMATION

Corresponding Author

Jae-Won Shin – Department of Pharmacology and Regenerative Medicine and Department of Biomedical Engineering, University of Illinois at Chicago, Chicago, Illinois 60612, United States; orcid.org/0000-0003-4823-6373; Email: shinwj@uic.edu

Authors

Stephen Lenzini – Department of Pharmacology and Regenerative Medicine and Department of Biomedical Engineering, University of Illinois at Chicago, Chicago, Illinois 60612, United States

Koushik Debnath – Department of Pharmacology and Regenerative Medicine and Department of Biomedical Engineering, University of Illinois at Chicago, Chicago, Illinois 60612, United States; orcid.org/0000-0003-4050-1187

Jagdish C. Joshi – Department of Pharmacology and Regenerative Medicine, University of Illinois at Chicago, Chicago, Illinois 60612, United States

Sing Wan Wong – Department of Pharmacology and Regenerative Medicine and Department of Biomedical Engineering, University of Illinois at Chicago, Chicago, Illinois 60612, United States

Kriti Srivastava – Department of Pharmacology and Regenerative Medicine, University of Illinois at Chicago, Chicago, Illinois 60612, United States

Xue Geng – Department of Biomedical Engineering, University of Illinois at Chicago, Chicago, Illinois 60612, United States

Ik Sung Cho – Department of Pharmacology and Regenerative Medicine and Department of Biomedical Engineering, University of Illinois at Chicago, Chicago, Illinois 60612, United States

Angela Song – Department of Pharmacology and Regenerative Medicine and Department of Biomedical Engineering, University of Illinois at Chicago, Chicago, Illinois 60612, United States

Raymond Bargi – Department of Pharmacology and Regenerative Medicine and Department of Biomedical Engineering, University of Illinois at Chicago, Chicago, Illinois 60612, United States

James C. Lee – Department of Biomedical Engineering, University of Illinois at Chicago, Chicago, Illinois 60612, United States; orcid.org/0000-0002-7173-4875

Gary C.H. Mo – Department of Pharmacology and Regenerative Medicine, University of Illinois at Chicago, Chicago, Illinois 60612, United States; orcid.org/0000-0002-3191-2155

Dolly Mehta – Department of Pharmacology and Regenerative Medicine, University of Illinois at Chicago, Chicago, Illinois 60612, United States

Complete contact information is available at:
<https://pubs.acs.org/10.1021/acsnano.1c03231>

Notes

The authors declare no competing financial interest.

ACKNOWLEDGMENTS

We acknowledge P. Toth from the Fluorescence Imaging Core, B. Ganesh from the Flow Cytometry Core, and F. Seiler from the Electron Microscopy Core at the University of Illinois at Chicago, as well as the Analytical bioNanoTechnology Core (ANTEC) at Northwestern University for their help and support. We thank S. Rayees and M.Z. Akhter from the laboratory of D. Mehta (UIC) for technical advice on a mouse model of acute lung injury. This work made use of instruments in the Fluorescence Imaging Core (Research Resources Center, UIC). This work was supported by National Institutes of Health Grant R01-HL141255 (J.-W.S.), R01-GM141147 (J.-W.S.), R00-HL125884 (J.-W.S.), R01-HL084153 (D.M.),

R01-AG044404 (J.C.L.), T32-HL07829 (S.L.), and American Heart Association Grant 19PRE34380087 (S.L.).

REFERENCES

- (1) Meldolesi, J. Exosomes and Ectosomes in Intercellular Communication. *Curr. Biol.* **2018**, *28* (8), R435–R444.
- (2) Mathieu, M.; Martin-Jaular, L.; Lavieu, G.; Thery, C. Specificities of Secretion and Uptake of Exosomes and Other Extracellular Vesicles for Cell-to-Cell Communication. *Nat. Cell Biol.* **2019**, *21* (1), 9–17.
- (3) van Niel, G.; D'Angelo, G.; Raposo, G. Shedding Light on the Cell Biology of Extracellular Vesicles. *Nat. Rev. Mol. Cell Biol.* **2018**, *19* (4), 213–228.
- (4) Wiklander, O. P. B.; Brennan, M. A.; Lotvall, J.; Breakefield, X. O.; El Andaloussi, S. Advances in Therapeutic Applications of Extracellular Vesicles. *Sci. Transl. Med.* **2019**, *11* (492), eaav8521.
- (5) Armstrong, J. P.; Holme, M. N.; Stevens, M. M. Re-Engineering Extracellular Vesicles as Smart Nanoscale Therapeutics. *ACS Nano* **2017**, *11* (1), 69–83.
- (6) Shao, C.; Yang, F.; Miao, S.; Liu, W.; Wang, C.; Shu, Y.; Shen, H. Role of Hypoxia-Induced Exosomes in Tumor Biology. *Mol. Cancer* **2018**, *17* (1), 120.
- (7) Verweij, F. J.; Bebelman, M. P.; Jimenez, C. R.; Garcia-Vallejo, J. J.; Janssen, H.; Neefjes, J.; Knol, J. C.; de Goeij-de Haas, R.; Piersma, S. R.; Baglio, S. R.; Verhage, M.; Middeldorp, J. M.; Zomer, A.; van Rheenen, J.; Coppelino, M. G.; Hurbain, I.; Raposo, G.; Smit, M. J.; Toonen, R. F. G.; van Niel, G.; et al. Quantifying Exosome Secretion from Single Cells Reveals a Modulatory Role for GPCR Signaling. *J. Cell Biol.* **2018**, *217* (3), 1129–1142.
- (8) Messenger, S. W.; Woo, S. S.; Sun, Z.; Martin, T. F. J. A Ca(2+)-Stimulated Exosome Release Pathway in Cancer Cells Is Regulated by Munc13–4. *J. Cell Biol.* **2018**, *217* (8), 2877–2890.
- (9) Witwer, K. W.; Van Balkom, B. W. M.; Bruno, S.; Choo, A.; Dominici, M.; Gimona, M.; Hill, A. F.; De Kleijn, D.; Koh, M.; Lai, R. C.; Mitsialis, S. A.; Ortiz, L. A.; Rohde, E.; Asada, T.; Toh, W. S.; Weiss, D. J.; Zheng, L.; Giebel, B.; Lim, S. K. Defining Mesenchymal Stromal Cell (MSC)-Derived Small Extracellular Vesicles for Therapeutic Applications. *J. Extracell. Vesicles* **2019**, *8* (1), 1609206.
- (10) Pittenger, M. F.; Discher, D. E.; Peault, B. M.; Phinney, D. G.; Hare, J. M.; Caplan, A. I. Mesenchymal Stem Cell Perspective: Cell Biology to Clinical Progress. *NPJ. Regen. Med.* **2019**, *4*, 22.
- (11) Tang, X. D.; Shi, L.; Monsel, A.; Li, X. Y.; Zhu, H. L.; Zhu, Y. G.; Qu, J. M. Mesenchymal Stem Cell Microvesicles Attenuate Acute Lung Injury in Mice Partly Mediated by Ang-1 mRNA. *Stem Cells* **2017**, *35* (7), 1849–1859.
- (12) Ahn, S. Y.; Park, W. S.; Kim, Y. E.; Sung, D. K.; Sung, S. I.; Ahn, J. Y.; Chang, Y. S. Vascular Endothelial Growth Factor Mediates the Therapeutic Efficacy of Mesenchymal Stem Cell-Derived Extracellular Vesicles against Neonatal Hyperoxic Lung Injury. *Exp. Mol. Med.* **2018**, *50* (4), 1–12.
- (13) Zhu, Y. G.; Feng, X. M.; Abbott, J.; Fang, X. H.; Hao, Q.; Monsel, A.; Qu, J. M.; Matthay, M. A.; Lee, J. W. Human Mesenchymal Stem Cell Microvesicles for Treatment of *Escherichia coli* Endotoxin-Induced Acute Lung Injury in Mice. *Stem Cells* **2014**, *32* (1), 116–25.
- (14) Monsel, A.; Zhu, Y. G.; Gennai, S.; Hao, Q.; Hu, S.; Rouby, J. J.; Rosenzweig, M.; Matthay, M. A.; Lee, J. W. Therapeutic Effects of Human Mesenchymal Stem Cell-Derived Microvesicles in Severe Pneumonia in Mice. *Am. J. Respir. Crit. Care Med.* **2015**, *192* (3), 324–36.
- (15) Chaubey, S.; Thuesen, S.; Ponnalagu, D.; Alam, M. A.; Gheorghe, C. P.; Aghai, Z.; Singh, H.; Bhandari, V. Early Gestational Mesenchymal Stem Cell Secretome Attenuates Experimental Bronchopulmonary Dysplasia in Part via Exosome-Associated Factor TSG-6. *Stem Cell Res. Ther.* **2018**, *9* (1), 173.
- (16) Park, J.; Kim, S.; Lim, H.; Liu, A.; Hu, S.; Lee, J.; Zhuo, H.; Hao, Q.; Matthay, M. A.; Lee, J. W. Therapeutic Effects of Human Mesenchymal Stem Cell Microvesicles in an *ex Vivo* Perfused Human Lung Injured with Severe *E. coli* Pneumonia. *Thorax* **2019**, *74* (1), 43–50.

- (17) Morrison, T. J.; Jackson, M. V.; Cunningham, E. K.; Kissenpfennig, A.; McAuley, D. F.; O'Kane, C. M.; Krasnodembskaya, A. D. Mesenchymal Stromal Cells Modulate Macrophages in Clinically Relevant Lung Injury Models by Extracellular Vesicle Mitochondrial Transfer. *Am. J. Respir. Crit. Care Med.* **2017**, *196* (10), 1275–1286.
- (18) Vining, K. H.; Mooney, D. J. Mechanical Forces Direct Stem Cell Behaviour in Development and Regeneration. *Nat. Rev. Mol. Cell Biol.* **2017**, *18* (12), 728–742.
- (19) Wong, S. W.; Lenzini, S.; Giovanni, R.; Knowles, K.; Shin, J. W. Matrix Biophysical Cues Direct Mesenchymal Stromal Cell Functions in Immunity. *Acta Biomater.* **2021**, *133*, 126.
- (20) Diz-Munoz, A.; Fletcher, D. A.; Weiner, O. D. Use the Force: Membrane Tension as an Organizer of Cell Shape and Motility. *Trends Cell Biol.* **2013**, *23* (2), 47–53.
- (21) Wong, S. W.; Lenzini, S.; Shin, J. W. Perspective: Biophysical Regulation of Cancerous and Normal Blood Cell Lineages in Hematopoietic Malignancies. *APL Bioeng* **2018**, *2* (3), 031802.
- (22) Wong, S. W.; Lenzini, S.; Cooper, M. H.; Mooney, D. J.; Shin, J. W. Soft Extracellular Matrix Enhances Inflammatory Activation of Mesenchymal Stromal Cells to Induce Monocyte Production and Trafficking. *Sci. Adv.* **2020**, *6* (15), No. eaaw0158.
- (23) Wong, S. W.; Lenzini, S.; Bargi, R.; Feng, Z.; Macaraniag, C.; Lee, J. C.; Peng, Z.; Shin, J. W. Controlled Deposition of 3D Matrices to Direct Single Cell Functions. *Adv. Sci. (Weinh)* **2020**, *7* (20), 2001066.
- (24) Wong, S. W.; Tamatam, C. R.; Cho, I. S.; Toth, P. T.; Bargi, R.; Belvitch, P.; Lee, J. C.; Rehman, J.; Reddy, S. P.; Shin, J. W. Inhibition of Aberrant Tissue Remodelling by Mesenchymal Stromal Cells Singly Coated with Soft Gels Presenting Defined Chemomechanical Cues. *Nat. Biomed Eng.* **2021** DOI: 10.1038/s41551-021-00740-x
- (25) Humphries, J. D.; Byron, A.; Humphries, M. J. Integrin Ligands at a Glance. *J. Cell Sci.* **2006**, *119*, 3901–3.
- (26) Zhao, X.; Huebsch, N.; Mooney, D. J.; Suo, Z. Stress-Relaxation Behavior in Gels with Ionic and Covalent Crosslinks. *J. Appl. Phys.* **2010**, *107* (6), 063509.
- (27) Lobb, R. J.; Becker, M.; Wen Wen, S.; Wong, C. S.; Wiegman, A. P.; Leimgruber, A.; Möller, A. Optimized Exosome Isolation Protocol for Cell Culture Supernatant and Human Plasma. *J. Extracell. Vesicles* **2015**, *4*, 27031.
- (28) Diduch, D. R.; Coe, M. R.; Joyner, C.; Owen, M. E.; Balian, G. Two Cell Lines from Bone Marrow That Differ in Terms of Collagen Synthesis, Osteogenic Characteristics, and Matrix Mineralization. *JBJS* **1993**, *75* (1), 92–105.
- (29) Kim, C.; Ye, F.; Ginsberg, M. H. Regulation of Integrin Activation. *Annu. Rev. Cell Dev. Biol.* **2011**, *27*, 321–45.
- (30) Pelham, R. J., Jr.; Wang, Y. Cell Locomotion and Focal Adhesions Are Regulated by Substrate Flexibility. *Proc. Natl. Acad. Sci. U. S. A.* **1997**, *94* (25), 13661–5.
- (31) Kong, F.; Garcia, A. J.; Mould, A. P.; Humphries, M. J.; Zhu, C. Demonstration of Catch Bonds between an Integrin and Its Ligand. *J. Cell Biol.* **2009**, *185* (7), 1275–84.
- (32) Mas-Moruno, C.; Rechenmacher, F.; Kessler, H. Cilengitide: The First Anti-Angiogenic Small Molecule Drug Candidate Design, Synthesis and Clinical Evaluation. *Anti-Cancer Agents Med. Chem.* **2010**, *10* (10), 753–768.
- (33) Lenzini, S.; Bargi, R.; Chung, G.; Shin, J. W. Matrix Mechanics and Water Permeation Regulate Extracellular Vesicle Transport. *Nat. Nanotechnol.* **2020**, *15* (3), 217–223.
- (34) Sinha, S.; Hoshino, D.; Hong, N. H.; Kirkbride, K. C.; Grega-Larson, N. E.; Seiki, M.; Tyska, M. J.; Weaver, A. M. Cortactin Promotes Exosome Secretion by Controlling Branched Actin Dynamics. *J. Cell Biol.* **2016**, *214* (2), 197–213.
- (35) Luby-Phelps, K.; Castle, P. E.; Taylor, D. L.; Lanni, F. Hindered Diffusion of Inert Tracer Particles in the Cytoplasm of Mouse 3T3 Cells. *Proc. Natl. Acad. Sci. U. S. A.* **1987**, *84* (14), 4910–3.
- (36) Gupta, M.; Sarangi, B. R.; Deschamps, J.; Nematbakhsh, Y.; Callan-Jones, A.; Margadant, F.; Mege, R. M.; Lim, C. T.; Voituriez, R.; Ladoux, B. Adaptive Rheology and Ordering of Cell Cytoskeleton Govern Matrix Rigidity Sensing. *Nat. Commun.* **2015**, *6*, 7525.
- (37) Oakes, P. W.; Bidone, T. C.; Beckham, Y.; Skeeters, A. V.; Ramirez-San Juan, G. R.; Winter, S. P.; Voth, G. A.; Gardel, M. L. Lamellipodium Is a Myosin-Independent Mechanosensor. *Proc. Natl. Acad. Sci. U. S. A.* **2018**, *115* (11), 2646–2651.
- (38) Serrels, B.; Serrels, A.; Brunton, V. G.; Holt, M.; McLean, G. W.; Gray, C. H.; Jones, G. E.; Frame, M. C. Focal Adhesion Kinase Controls Actin Assembly via a Form-Mediated Interaction with the Arp2/3 Complex. *Nat. Cell Biol.* **2007**, *9* (9), 1046–56.
- (39) Xu, K.; Zhong, G.; Zhuang, X. Actin, Spectrin, and Associated Proteins Form a Periodic Cytoskeletal Structure in Axons. *Science* **2013**, *339* (6118), 452–6.
- (40) Mo, G. C.; Ross, B.; Hertel, F.; Manna, P.; Yang, X.; Greenwald, E.; Booth, C.; Plummer, A. M.; Tenner, B.; Chen, Z.; Wang, Y.; Kennedy, E. J.; Cole, P. A.; Fleming, K. G.; Palmer, A.; Jimenez, R.; Xiao, J.; Dedeker, P.; Zhang, J. Genetically Encoded Biosensors for Visualizing Live-Cell Biochemical Activity at Super-Resolution. *Nat. Methods* **2017**, *14* (4), 427–434.
- (41) Pan, L.; Yan, R.; Li, W.; Xu, K. Super-Resolution Microscopy Reveals the Native Ultrastructure of the Erythrocyte Cytoskeleton. *Cell Rep.* **2018**, *22* (5), 1151–1158.
- (42) Sheetz, M. P. Cell Control by Membrane-Cytoskeleton Adhesion. *Nat. Rev. Mol. Cell Biol.* **2001**, *2* (5), 392–6.
- (43) Askarova, S.; Sun, Z.; Sun, G. Y.; Meininger, G. A.; Lee, J. C. Amyloid-Beta Peptide on Sialyl-Lewis(X)-Selectin-Mediated Membrane Tether Mechanics at the Cerebral Endothelial Cell Surface. *PLoS One* **2013**, *8* (4), No. e60972.
- (44) Sun, M.; Graham, J. S.; Hegedus, B.; Marga, F.; Zhang, Y.; Forgacs, G.; Grandbois, M. Multiple Membrane Tethers Probed by Atomic Force Microscopy. *Biophys. J.* **2005**, *89* (6), 4320–9.
- (45) Teng, T.; Dong, L.; Ridgley, D. M.; Ghura, S.; Tobin, M. K.; Sun, G. Y.; LaDu, M. J.; Lee, J. C. Cytosolic Phospholipase A2 Facilitates Oligomeric Amyloid-Beta Peptide Association with Microglia via Regulation of Membrane-Cytoskeleton Connectivity. *Mol. Neurobiol.* **2019**, *56* (5), 3222–3234.
- (46) Abraham, A.; Krasnodembskaya, A. Mesenchymal Stem Cell-Derived Extracellular Vesicles for the Treatment of Acute Respiratory Distress Syndrome. *Stem Cells Transl. Med.* **2020**, *9* (1), 28–38.
- (47) Matthay, M. A. Extracellular Vesicle Transfer from Mesenchymal Stromal Cells Modulates Macrophage Function in Acute Lung Injury. Basic Science and Clinical Implications. *Am. J. Respir. Crit. Care Med.* **2017**, *196* (10), 1234–1236.
- (48) Ragni, E.; Banfi, F.; Barilani, M.; Cherubini, A.; Parazzi, V.; Larghi, P.; Dolo, V.; Bollati, V.; Lazzari, L. Extracellular Vesicle-Shuttled mRNA in Mesenchymal Stem Cell Communication. *Stem Cells* **2017**, *35* (4), 1093–1105.
- (49) Song, Y.; Dou, H.; Li, X.; Zhao, X.; Li, Y.; Liu, D.; Ji, J.; Liu, F.; Ding, L.; Ni, Y.; Hou, Y. Exosomal Mir-146a Contributes to the Enhanced Therapeutic Efficacy of Interleukin-1 β -Primed Mesenchymal Stem Cells against Sepsis. *Stem Cells* **2017**, *35* (5), 1208–1221.
- (50) Yi, X.; Wei, X.; Lv, H.; An, Y.; Li, L.; Lu, P.; Yang, Y.; Zhang, Q.; Yi, H.; Chen, G. Exosomes Derived from MicroRNA-30b-3p-Overexpressing Mesenchymal Stem Cells Protect against Lipopolysaccharide-Induced Acute Lung Injury by Inhibiting Saa3. *Exp. Cell Res.* **2019**, *383* (2), 111454.
- (51) Wang, J.; Huang, R.; Xu, Q.; Zheng, G.; Qiu, G.; Ge, M.; Shu, Q.; Xu, J. Mesenchymal Stem Cell-Derived Extracellular Vesicles Alleviate Acute Lung Injury via Transfer of Mir-27a-3p. *Crit. Care Med.* **2020**, *48* (7), e599–e610.
- (52) Jeppesen, D. K.; Fenix, A. M.; Franklin, J. L.; Higginbotham, J. N.; Zhang, Q.; Zimmerman, L. J.; Liebler, D. C.; Ping, J.; Liu, Q.; Evans, R.; et al. Reassessment of Exosome Composition. *Cell* **2019**, *177* (2), 428–445.e18.
- (53) Turegano-Lopez, M.; Santuy, A.; DeFelipe, J.; Merchan-Perez, A. Size, Shape, and Distribution of Multivesicular Bodies in the Juvenile Rat Somatosensory Cortex: A 3D Electron Microscopy Study. *Cereb. Cortex* **2020**, *30* (3), 1887–1901.

- (54) Adell, M. A.; Vogel, G. F.; Pakdel, M.; Muller, M.; Lindner, H.; Hess, M. W.; Teis, D. Coordinated Binding of Vps4 to ESCRT-III Drives Membrane Neck Constriction during MVB Vesicle Formation. *J. Cell Biol.* **2014**, *205* (1), 33–49.
- (55) Fermie, J.; Liv, N.; Ten Brink, C.; van Donselaar, E. G.; Muller, W. H.; Schieber, N. L.; Schwab, Y.; Gerritsen, H. C.; Klumperman, J. Single Organelle Dynamics Linked to 3D Structure by Correlative Live-Cell Imaging and 3D Electron Microscopy. *Traffic* **2018**, *19* (5), 354–369.
- (56) Guo, M.; Pegoraro, A. F.; Mao, A.; Zhou, E. H.; Arany, P. R.; Han, Y.; Burnette, D. T.; Jensen, M. H.; Kasza, K. E.; Moore, J. R.; Mackintosh, F. C.; Fredberg, J. J.; Mooney, D. J.; Lippincott-Schwartz, J.; Weitz, D. A. Cell Volume Change through Water Efflux Impacts Cell Stiffness and Stem Cell Fate. *Proc. Natl. Acad. Sci. U. S. A.* **2017**, *114* (41), E8618–E8627.
- (57) Mogre, S.; Brown, A. I.; Koslover, E. F. Getting around the Cell: Physical Transport in the Intracellular World. *Phys. Biol.* **2020**, *17*, 061003.
- (58) Lenzini, S.; Devine, D.; Shin, J. W. Leveraging Biomaterial Mechanics to Improve Pluripotent Stem Cell Applications for Tissue Engineering. *Front. Bioeng. Biotechnol.* **2019**, *7*, 260.
- (59) Burdick, J. A.; Murphy, W. L. Moving from Static to Dynamic Complexity in Hydrogel Design. *Nat. Commun.* **2012**, *3*, 1269.
- (60) Whitford, W.; Guterstam, P. Exosome Manufacturing Status. *Future Med. Chem.* **2019**, *11* (10), 1225–1236.
- (61) Wiest, E. F.; Zubair, A. C. Challenges of Manufacturing Mesenchymal Stromal Cell-Derived Extracellular Vesicles in Regenerative Medicine. *Cytotherapy* **2020**, *22* (11), 606–612.
- (62) Ng, K. S.; Smith, J. A.; McAteer, M. P.; Mead, B. E.; Ware, J.; Jackson, F. O.; Carter, A.; Ferreira, L.; Bure, K.; Rowley, J. A.; Reeve, B.; Brindley, D. A.; Karp, J. M. Bioprocess Decision Support Tool for Scalable Manufacture of Extracellular Vesicles. *Biotechnol. Bioeng.* **2019**, *116* (2), 307–319.
- (63) Wang, J.; Bonacquisti, E. E.; Brown, A. D.; Nguyen, J. Boosting the Biogenesis and Secretion of Mesenchymal Stem Cell-Derived Exosomes. *Cells* **2020**, *9* (3), 660.
- (64) Colao, I. L.; Corteling, R.; Bracewell, D.; Wall, I. Manufacturing Exosomes: A Promising Therapeutic Platform. *Trends Mol. Med.* **2018**, *24* (3), 242–256.
- (65) Watson, D. C.; Yung, B. C.; Bergamaschi, C.; Chowdhury, B.; Bear, J.; Stellas, D.; Morales-Kastresana, A.; Jones, J. C.; Felber, B. K.; Chen, X.; Pavlakis, G. N. Scalable, Cgmp-Compatible Purification of Extracellular Vesicles Carrying Bioactive Human Heterodimeric IL-15/Lactadherin Complexes. *J. Extracell. Vesicles* **2018**, *7* (1), 1442088.
- (66) Yang, Z.; Shi, J.; Xie, J.; Wang, Y.; Sun, J.; Liu, T.; Zhao, Y.; Zhao, X.; Wang, X.; Ma, Y.; Malkoc, V.; Chiang, C.; Deng, W.; Chen, Y.; Fu, Y.; Kwak, K. J.; Fan, Y.; Kang, C.; Yin, C.; Rhee, J.; et al. Large-Scale Generation of Functional mRNA-Encapsulating Exosomes via Cellular Nanoporation. *Nat. Biomed Eng.* **2020**, *4* (1), 69–83.
- (67) Zhang, H.; Lyden, D. Asymmetric-Flow Field-Flow Fractionation Technology for Exomere and Small Extracellular Vesicle Separation and Characterization. *Nat. Protoc.* **2019**, *14* (4), 1027–1053.
- (68) Yang, L. H.; Wang, S. L.; Tang, L. L.; Liu, B.; Ye, W. L.; Wang, L. L.; Wang, Z. Y.; Zhou, M. T.; Chen, B. C. Universal Stem-Loop Primer Method for Screening and Quantification of MicroRNA. *PLoS One* **2014**, *9* (12), No. e115293.
- (69) Devine, D.; Vijayakumar, V.; Wong, S. W.; Lenzini, S.; Newman, P.; Shin, J. W. Hydrogel Micropost Arrays with Single Post Tunability to Study Cell Volume and Mechanotransduction. *Adv. Biosyst* **2020**, *4* (11), No. 2000012.
- (70) Rahbek-Clemmensen, T.; Lycas, M. D.; Erlendsson, S.; Eriksen, J.; Apuschkin, M.; Vilhardt, F.; Jorgensen, T. N.; Hansen, F. H.; Gether, U. Super-Resolution Microscopy Reveals Functional Organization of Dopamine Transporters into Cholesterol and Neuronal Activity-Dependent Nanodomains. *Nat. Commun.* **2017**, *8* (1), 740.
- (71) Knezevic, N.; Tauseef, M.; Thennes, T.; Mehta, D. The G Protein Betagamma Subunit Mediates Reannealing of Adherens Junctions to Reverse Endothelial Permeability Increase by Thrombin. *J. Exp. Med.* **2009**, *206* (12), 2761–77.